# Master of Science Thesis

# Monte Carlo simulation with Geant4 for verification of rotational total skin electron therapy (TSET)

Christina Zacharatou Jarlskog

Supervisors: Sven ÅJ Bäck,

Joakim Medin, Lena Wittgren

# TABLE OF CONTENTS

# ABSTRACT

*Background and purpose*: This study refers to a rotational radiotherapy technique for the treatment of mycosis fungoides. Patients are irradiated by a high dose-rate low-energy electron beam while they stand on a rotating platform. This report presents a first effort to use the Geant4 simulation program to calculate the relation between the stationary and rotational depth dose distributions in an ellipsoid phantom along the central beam axis. The absorbed dose delivered in one rotation can then be inferred from dose rate measurements performed in a stationary geometry.

*Method*: Percentage depth dose and ionisation chamber measurements along the central beam axis were done at SSD = 100 cm and 250 cm (treatment distance). The measurement at SSD = 100 cm was used 1. to extract the beam characterization using VMC++ calculated percentage depth dose distributions and 2. to select the physics model of Geant4. A set of simulations were subsequently performed at the treatment distance in order to determine the following parameters in the simulation: 1. the number of primary electrons that are needed for the calculation of the ratio between the stationary and rotational depth dose distributions, $R$, to have a given level of statistical uncertainty (2%), 2. the distance off the central beam axis within which the energy should be scored, $r$, and 3. the step in beam incidence angle, $\Delta \vartheta$. The rotational depth dose and $R$ distributions were then calculated for one elliptical and one cylindrical phantom. The cylindrical phantom calculations were done for two production thresholds for the electrons, 10 keV and 100 keV.

*Results*: This simulation study has contributed to the theoretical background of a rotational technique for total skin electron therapy (TSET). It was found that the low production threshold simulations give results that agree better with the measurements and the VMC++ calculation at SSD = 100 cm and also with the expected shape of the depth dose distribution for one rotation.

*Conclusion*: The Monte Carlo calculations presented in this report were used to determine the the relation between the stationary and rotational depth dose distributions and thus contributed to a more accurate evaluation of the absorbed dose delivered at the prescription depth during treatment.

# POPULÄRVETENSKAPLIG SAMMANFATTNING

## Datorsimuleringar för helkroppsbehandling med elektronstrålning

Detta arbete handlar om en behandlingsteknik för hudterapi där lågenergetiska elektroner utnyttjas för strålbehandling där patienten står eller sitter på en roterande plattform. För att behandlingen skall få ett lyckat resultat krävs en viss stråldos (den absorberade energin per massenhet) till patientens hud. För att kontrollera att dosen är rätt används normalt mätningar med olika detektorer. Dessa detektorer fungerar optimalt när de är riktade mot strålkällan men har en obestämd känslighet när de roteras. Målet med detta arbetet var att uppskatta den totala dosen under en rotation genom att använda ett datorsimuleringsprogram (Geant4).

Programmet Geant4, för simulering av transport av partiklar i materia, utnyttjas av ett brett spektrum av användare inom högenergifysiken, rymdfysiken och för medicinska ändamål. Programmet har nyligen uppdaterats med nya rutiner för elektromagnetisk strålning (jonisation, bromsstrålning och multipelspridning) vilket har ökat precisionen av simuleringar för rymd- och medicinska applikationer. Ett stort antal användare i Europa utnyttjar nu programmet för beräkningar av lågenergetiska elektromagnetiska processer och i denna studie har vi använt programmet för att simulera behandlingstekniken som nämndes ovan.

Resultaten av denna undersökning visar att Geant4 programmet ger god överensstämmelse i en stillastående referensgeometri när man jämför med mätningar och med ett annat simuleringsprogram (VMC++).

Resultaten visar också att Geant4 kan optimeras för beräkningar även vid mycket låga energier, och att programmet kan användas för att bestämma dosfördelningen när patienten roterar.

Sammanfattningsvis, i detta arbete har vi visat att Monte Carlo beräkningar kan användas för att förbättra noggrannhet vid bestämning av dosen som patienten får.

# 1  INTRODUCTION

## 1.1  Total skin electron beam therapy

Total skin electron therapy (TSET) [1] has been used for the treatment of cutaneous diseases such as mycosis fungoides (T-cell lymphoma) and other cutaneous lymphomas for the past fifty years. Mycosis fungoides was the first of these malignancies to be treated by ionizing radiation as early as 1902. The initial use of X-ray beams was soon found to induce severe adverse effects such as bone marrow suppression and even though mycosis fungoides responds equally well to photons and to electrons, electron beams were preferred for their superficial penetrability.

There are two groups of total-skin treatment techniques [2]: translational techniques and large field techniques. In translational techniques, the patient is placed in a horizontal position and is then translated with respect to a beam whose dimensions cover the patient laterally. In large field techniques, the patient is usually irradiated standing upright in the path of one or more fields, aiming to cover the upper and lower parts of the body.

A number of large-field treatment techniques have been developed, some of which are very complex and time-consuming. Static many-field techniques involve the irradiation of the patient by a number of angled beam pairs (dual fields). Each beam pair irradiates the patient at a stationary position. Each beam in the pair covers one part of the patient's body (one 'upper' beam and one 'lower' beam). The most common technique is the Stanford technique, which uses six dual fields. Alternatively, rotational techniques can be used [3, 4, 5], in which the patient is placed on a platform that rotates continuously in a single field or in a pair of angled fields.

Static techniques have been reported not to always produce a uniform dose distribution over the entire skin surface [6, 7]. Two-field treatments lead to flank recurrence because of underdosage in the electron field periphery and four-field treatments produce hot spots over the extremities because of field overlapping. These overdosed or underdose regions can be significantly eliminated using a six-field technique but this has a limitation in accurately producing the correct angles of incidence as this depends on proper positioning of the patient in six different postures. Techniques with eight or twelve fields have also been used but they entail a poor set-up reproducibility and time-consuming positioning of the patient, like in six-field treatment.

The present study refers to a rotational technique for total skin irradiation, which is used at Malmö University Hospital (UMAS). The electron beam is delivered by a Varian Clinac 2100C/D accelerator. For skin irradiation, the accelerator operates at a high dose rate mode allowing for short treatment times even at large source-to-surface distances. One or more fields can be used covering the upper, central or lower parts of the body. The treatment setup is shown in figure 1.1.

The electron beam is not collimated by an applicator but a special insert is used instead ('HDTSe-', figure 1.2), which is preset via interlock to maximum field size (36 cm x 36 cm at the isocenter) and 6 MeV energy. The insert is placed at the block holder of the gantry as shown in figure 1.3. Depending on the thickness of the lesions, treatment is done either with the nominal beam or with a degraded beam, which is obtained by placing a 6 mm thick plexiglass degrader at the gantry (figure 1.3). Apart from reducing the energy of the beam, the degrader is also used to scatter the electrons at wider angles. A second plexiglass plate of 2.5 cm thickness is sometimes placed in front of the patient to shield areas that should not be irradiated. The present study concentrates on a single horizontal field and a treatment distance of 250 cm.

**Figure 1.1.** Setup for total skin rotational treatment. The patient is irradiated standing on a platform which rotates at a speed of 3.3 revolutions per minute.



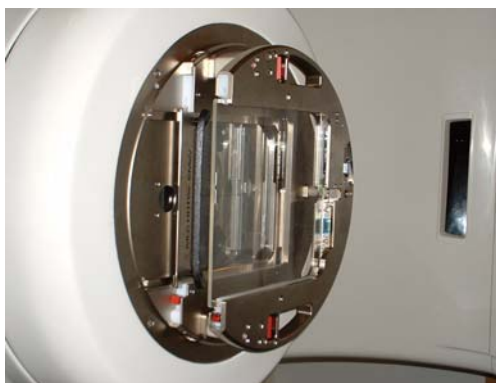**Figure 1.2.** Insert for high dose-rate 6 MeV electron irradiation.



**Figure 1.3.** The HDTSe⁻ insert and the degrader plate are placed at the block holder of the gantry.

## 1.2 Aim of this study

This study was initiated by the need for an accurate calculation of the rotational depth dose distribution in TSET dosimetry.

In a previous UMAS study [8], a number of measurements were done using a rotating phantom (cylinder of 30 cm diameter) and various detectors (ionisation chambers, diodes and TLDs) placed close to the surface of the phantom in order to determine the absorbed dose delivered in one rotation. The study showed that measuring in a rotational geometry entails a number of limitations emerging from detector size and the dependence of the response of the detectors on the angle of incidence of the beam [5].

The aim of this report is to present a first effort to use the simulation program Geant4 to determine the absorbed dose distribution along the central beam axis for one rotation and relate it to the corresponding absorbed dose distribution in a stationary geometry. Dose rate measurements in a stationary geometry at the treatment distance can then be used to determine the absorbed dose delivered in one rotation.

## 1.3 Calculation of the rotational depth dose distribution

For the sake of continuity, this study uses the following definition of [8]:

$$R = \frac{\text{dose in a stationary geometry for 100 MU}}{\text{dose in one rotation}} \tag{1.1}$$

The quantity $R$ is used to calculate the absorbed dose in one rotation assuming that the absorbed dose in the stationary geometry is measured for a given time interval (taken to be 100 MU). In this calculation, it is assumed that the dose rate of the accelerator remains constant with time.

As we have 888 MU/min and the platform speed is 3.3 rotations/min, one rotation corresponds to 270 monitor units (MU). If the angle between the beam direction and the phantom main axis is $\vartheta$, from eq. 1.1, it follows that

$$R_{MC} = \frac{100}{270} \frac{D_{MC}^{stationary}}{D_{MC}^{rotation}} \tag{1.2}$$

where $D_{MC}^{stationary}$ is the calculated depth dose distribution corresponding to $\vartheta = 0°$ and $D_{MC}^{rotation}$ is the calculated depth dose distribution for one rotation.

The calculation of $D_{MC}^{rotation}$ should be done by integration over all incidence angles, i.e.

$$D_{MC}^{rotation} = \int_{\vartheta} D(z, \vartheta) d\vartheta \tag{1.3}$$

where the integral is calculated from $\vartheta = 0°$ to $\vartheta = 360°$. Instead of performing the integration, $D_{MC}^{rotation}$ can be calculated approximately as a sum over discrete $\vartheta$ values

$$D_{MC}^{rotation} \cong w_{0°} D_{MC}^{\vartheta = 0°} + 2 \sum_{\vartheta} w_{\vartheta} D_{MC}^{0° < \vartheta \leq 90°} + 2 \sum_{\vartheta} w_{\vartheta} D_{MC}^{90° < \vartheta < 180°} + w_{180°} D_{MC}^{\vartheta = 180°} \tag{1.4}$$

where $D_{MC}^{\vartheta}$ is the simulated depth dose distribution for incidence angle $\vartheta$ and $w_{\vartheta}$ is a weight factor that shows what the contribution of each $D_{MC}^{\vartheta}$ is to the total $D_{MC}^{rotation}$ distribution. For simplicity, the factors $w_{\vartheta}$ can be taken to be independent of the angle $\vartheta$, which can be achieved by running the

simulations with equal spacing in $\vartheta$. The calculation of $D_{MC}^{rotation}$ can be further simplified by assuming that the contribution of angles $\vartheta > 90°$ can be neglected, from which it follows that

$$D_{MC}^{rotation} \cong w \left( D_{MC}^{\vartheta = 0°} + 2 \sum_{\vartheta} D_{MC}^{0° < \vartheta \le 90°} \right) \tag{1.5}$$

Assuming that the depth dose distributions in eq. 1.5 are normalized to the number of events, each term in the sum contributes with a weight factor

$$w = \frac{\Delta \vartheta}{360°} \tag{1.6}$$

where $\Delta \vartheta$ is the angle step in the simulations (in degrees). We thus have

$$D_{MC}^{rotation} \cong \frac{\Delta \vartheta}{360°} \left( D_{MC}^{\vartheta = 0°} + 2 \sum_{\vartheta} D_{MC}^{0° < \vartheta \le 90°} \right) \tag{1.7}$$

and

$$R_{MC} = \frac{100}{270} \frac{D_{MC}^{\vartheta = 0°}}{\frac{\Delta \vartheta}{360°} \left( D_{MC}^{\vartheta = 0°} + 2 \sum_{\vartheta} D_{MC}^{0° < \vartheta \le 90°} \right)} \tag{1.8}$$

The weight factor $w$ shows the fraction of time by which each beam angle contributes to the absorbed dose delivered in one rotation, so that $w \cdot 270$ is the number of MU corresponding to each angle of beam incidence $\vartheta$.

# 2  THE SIMULATION

## 2.1  Geant4 overview

The acronym 'Geant' was invented in the 1970's to name a code that simulated 'Ge'ometry 'an'd 't'racking for particle physics experiments. The first widely-used released version of the code, GEANT3, was written in FORTRAN and used several, at the time well-established, physics routines to model the physics of the interactions. As the complexity of the code kept increasing, object-oriented techniques were opted for instead, as this seemed to be the most efficient way to maintain the transparency of the code without compromising its performance. At that point it was also decided that the program would be given the form of a toolkit allowing the user to easily extend the components of all domains. This new phase of development led, in 1998, to the first production release of Geant4 [9], a C++ program that nowadays begins to be adopted by fields other than particle physics, such as space science and medical physics [10].

A Geant4 simulation run can be thought of as proceeding through the following steps (schematically shown in the appendix):

- the particles to be used are specified,
- the processes a particle is allowed to undergo are specified,
- the model describing each process is chosen,
- the materials to be used in the run are defined,
- the geometry of the system is defined,
- materials are assigned to the components of the geometry,
- external electromagnetic fields are defined,
- the sensitive detector components are specified,
- the response of the detectors is modelled,
- the primary events are generated (by e.g. an interface to an event generator),
- the primary particles are transported through the system and the production of secondary particles is simulated as they interact with matter,
- the event data (as 'measured' by the 'detectors') are stored for further analysis (e.g. in the form of histograms).

In the present application, there are no external electromagnetic fields and there is no issue of 'detector' response. The remaining components of the simulation are discussed in the following sections.

## 2.2  The definition of the geometry

There are two landmarks used in defining the geometry of the setup in Geant4: the 'World' volume and the internal reference frame of the simulation. The 'World' volume is conceived as the volume that includes all the three-dimensional space that the simulation has to consider. The internal reference frame of Geant4 is a Cartesian system that has its origin at the centre of the 'World', as shown in figure 2.1. Each component of the system is defined as a geometrical volume whose center is placed at a point in the reference frame of another volume.

When all volumes are thus placed, they are assigned materials. These are defined as elements or compounds. Compounds are defined by their atomic composition as given by a chemical formula or weight fractions, their density at a given temperature and pressure and their mean excitation energy.

In general, the term 'geometry' in Geant4 refers to the volumes built in the simulation, whether these are sensitive components registering hits or merely pieces of material the particles traverse. The part of the system that generates the primary particles is not included in the 'geometry' definition but in the 'primary event definition'. This convention in terminology is used in the rest of this report.

In the present application, the geometry consists in a homogeneous water volume whose shape varied between runs. In the stationary geometry runs, the phantom shape was a cube with 50 cm side. In the rotational geometry calculations, the phantom was an ellipsoid, as shown in figure 2.1, or a cylinder.
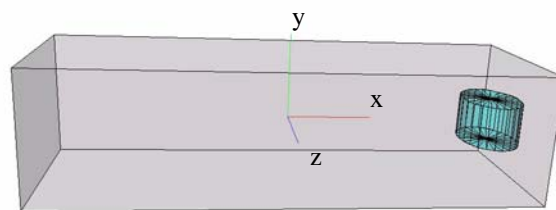


**Figure 2.1.**   Example of a geometry in Geant4. The axes of the internal reference system are shown.

## 2.3   Generating the primary events

This part of the simulation consists in defining the initial state of the simulation, i.e. the 'primary particles'. Once this is done, Geant4 will track the particles through the system (following the definition of physics processes) until they stop, decay or are transported beyond the limits of the World.

The generation of the primary event can be done using an interface to an event generator or the particle gun class, which creates a beam of particles by defining their type, position, direction of motion and kinetic energy. The generation of the primary event in the present application was done by using the latter option. The beam description was derived [11] using the coupled multi-source electron beam phase space model implemented in the Oncentra Treatment Planning system (OTP). In this derivation, it was assumed that the accelerator head geometry included a 25x25 cm$^2$ applicator as this was the best approximation for the treatment field.

The electron phase space was generated [11] by employing the OTP electron beam model and considering only the direct electrons, i.e. disregarding electrons out-scattered from collimating structures. Based on an earlier characterization of the electron phase space from a Clinac 2100C/D accelerator it was assumed that the phase space plane and the virtual source position were located 5 cm and 84.7 cm upstream the isocenter, respectively. A correction for multiple scatter in air in the treatment head was applied by a Gaussian distributed angular deflection with an RMS deflection angle that was independent of the generation coordinates of the electron.

A test run simulating 10 million 'OTP electrons' was made to score the parameters of the primary generation. The results are given in figures 2.2 and 3.4(b). The distributions are normalized to the total number of events.

Figure 2.2 shows the polar angle distribution (with respect to the central beam axis) before and after the correction for the interactions in the accelerator. The distribution reflects the rectangular shape of the field. The simulated field size was 36x36 cm$^2$, which gave a generation area of 33.25x33.25 cm$^2$. Since the generation position was sampled from a constant probability density distribution, the distribution of the polar angle has a linear rise from $0°$ to $11.8°$. The corners of the field contribute to an additional extent of the polar angle up to $16.7°$.

The calculation of the beam energy spectrum is discussed in section 3.3.
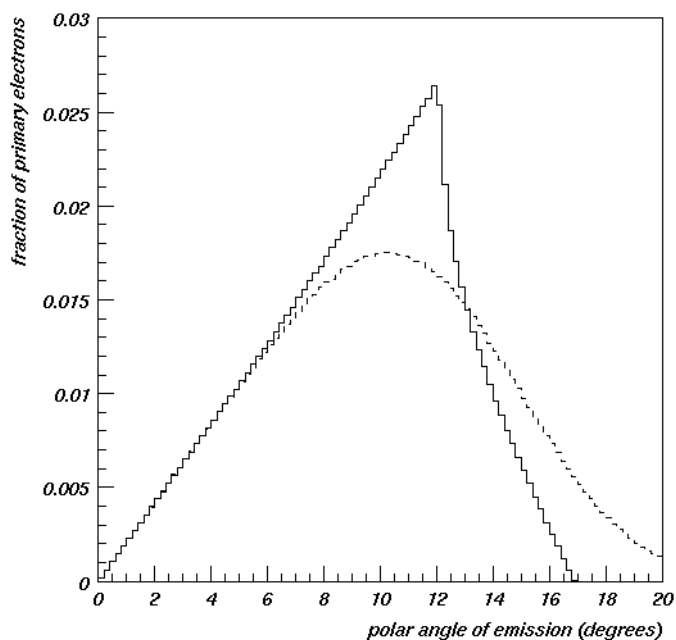


**Figure 2.2.** Distributions of the polar angle of emission before (solid line) and after (dashed line) the correction for interactions in the accelerator (calculated, this study).

## 2.4 Electromagnetic physics

The simulation proceeds by steps and the purpose of the implementation of the physics is to decide where these steps take place and which interactions are to be invoked at each step. This is done by using pseudorandom numbers which are uniformly distributed in the interval (0,1) to calculate the 'mean free path' or 'interaction length' for each interaction that the particle is allowed to undergo. The interaction that proposes the shortest mean free path is chosen. The step length can also be restricted to preserve precision or to prevent the particle from crossing a boundary in the geometry in a single step. The user can also request a maximum allowed step in the calculations. This latter option was not used in the runs described here but the calculations were rather determined only by the properties of the physics implementation.

The processes taken into account in the present application were only the electromagnetic ones since a 6-MeV electron beam cannot induce nuclear reactions. There are two models for electromagnetic physics in Geant4: the 'standard' model and the 'low-energy' model. By 'low-energy' is meant the regime below 100 GeV, in which respect both models are, in principle, applicable in the present context.

In the following, a short description of both physics models is given after a small note is made on the use of production cuts in Geant4. Emphasis is put on the low-energy physics classes, as these were used for the majority of the calculations (the reason for this choice is discussed in the next chapter). Only the interactions that were considered in the present simulations are discussed. A complete description of the physics used in Geant4 can be found in [12]. Overview reports of the physics models and their validation are given e.g. in [13, 14, 15, 16].

In the following, the term 'process' will be used in a general way, so as to denote either a physics process or an implementation of a physics interaction or model, or, in general, a class in the physics packages.

### 2.4.1 Production cuts

As was previously mentioned, Geant4 does not use tracking cuts, i.e. all particles are tracked to zero kinetic energy unless they reach the limits of the World. Photons and secondary electrons are, however, generated only above a given kinetic energy threshold ('production cut-off'). This is done as to avoid the production of a large number of secondary particles, which would deteriorate the performance of the simulation without enhancing the accuracy of the calculations.

In principle, production cuts can be applied to all processes but this is not done in practice. Instead, they are used to restrict only the generation of secondary particles by ionisation and bremsstrahlung. In the present study, the production threshold for photons was 10 keV in air and in water and the production threshold for electrons was 10 keV in air and 10 keV or 100 keV in water. The electron cut of 100 keV in water implies an uncertainty of about 150 μm in the calculation of the energy depositions in the simulation. These were scored with a binning of 500 μm in the present runs, which might introduce binning effects in the calculations (such effects have not been evaluated in this study).

### 2.4.2 Standard electromagnetic physics

In general, the standard electromagnetic physics model of Geant4 covers the energy range from 10 keV to several PeV and is mainly used for high-energy and nuclear physics applications.

In the standard electromagnetic physics model, the photon induced processes are Compton scattering, photon conversion and photoelectric effect. The electron/positron induced processes are ionisation, bremsstahlung and positron-electron annihilation. The 'ionisation' class for electrons and positrons calculates the continuous energy loss due to ionisation and simulates the 'discrete' part of the ionisation, i.e. Moller scattering, Bhabha scattering and δ-ray production. The bremsstrahlung class calculates the continuous energy loss due to soft bremsstrahlung and simulates 'discrete' bremsstrahlung.

The multiple scattering model is based on the Lewis theory [17]. This model is a condensed multiple scattering algorithm which is invoked at the end of the step to compute a correction to the mean path length and also the lateral displacement of the track. The model uses functions to determine the angular and spatial distributions after the step. The functions are chosen as to give the same moments of the angular and spatial distributions as the Lewis theory.

A special case of 'process' in Geant4 is the 'transportation' process. This class is responsible for determining the geometrical limits of a step and handles the crossing of geometric boundaries. It calculates the distance to the next volume in the geometry and proposes this distance as a possible step length in the same way as the physics processes propose the 'physical' step lengths using their cross sections. The transportation process requires that the particle should always stop at a boundary, thus setting an additional restriction on the step length, as was mentioned above.

### 2.4.3 Low-energy electromagnetic physics

The low-energy electromagnetic physics package is an extension to the standard physics code and uses shell cross section data rather than their parametrizations (as they are used in the standard model). A lowest validity limit of 250 eV was chosen to allow for the treatment of characteristic K-shell emission down to Z=6. The model covers the interactions of photons and electrons in materials with atomic number between 1 and 100. This package does not provide a new implementation of processes induced by positrons. They are treated by the same classes as in the standard electromagnetic physics package. The extended classes of the model treat the following interactions: Compton scattering, Rayleigh scattering, photoelectric effect, ionisation and bremsstrahlung. Photon conversion has also been implemented with the same methodology for the total cross section calculation as the processes above. The model also provides implementations for atomic relaxation (fluorescence and Auger electrons).

The implementation of all processes is done in two phases: (a) calculation of the total cross sections and (b) generation of the final state. Both phases are based on data from the following libraries: Evaluated Photon Data Library (EPDL) [18], Evaluated Electron Data Library (EEDL) [19] and Evaluated Atomic Data Library (EADL) [20].

The energy dependence of the total cross section is derived for each process from the evaluated data libraries. The total cross-section at a given energy is calculated by interpolation between the closest lower and higher energies for which data are available [21]:

$$\log(\sigma(E)) = \log(\sigma_1)\frac{\log(E_2)-\log(E)}{\log(E_2)-\log(E_1)} + \log(\sigma_2)\frac{\log(E)-\log(E_1)}{\log(E_2)-\log(E_1)} \qquad (2.1)$$

The final state is defined by the four-momenta of the final state products. These are determined according to distributions derived from the evaluated data.

### Compton scattering

The total cross section at energy $E$ is calculated by eq. 2.1. The scattered photon energy is sampled using the distribution

$$P(\varepsilon, q) = \Phi(\varepsilon) \cdot F(q) \qquad (2.2)$$

where $\Phi(\varepsilon)$ is the Klein-Nishina formula

$$\Phi(\varepsilon) \cong \left(\frac{1}{\varepsilon} + \varepsilon\right)\left(1 - \frac{\varepsilon\sin^2(\theta)}{1+\varepsilon^2}\right) \qquad (2.3)$$

$F(q)$ are scattering functions, $\varepsilon$ is the ratio between the scattered photon energy and the incident photon energy, $\theta$ is the scattering angle and $q$ is the momentum transfer

$$q = E\sin^2(\theta/2) \qquad (2.4)$$

The form factors are calculated from the data in the EPDL library. The angular distribution of the scattered photon is obtained in the same way.

### Rayleigh scattering

The total cross section at energy $E$ is calculated by eq. 2.1. The angular distribution of the scattered photon is given by the relation

$$\Phi(E, \theta) = [1 + \cos^2(\theta)]F^2(q) \tag{2.5}$$

where $q$ is the momentum transfer (eq. 2.4) and $F(q)$ is a form factor obtained from the EPDL library.

### Photoelectric effect

The total cross section at kinetic energy $T$ is calculated by eq. 2.1. The cross sections of the subshells are calculated in the same way and they are used to select the subshell from which the electron will be emitted. The electron is emitted at the direction of the incident photon. The interaction leaves the atom in an excited state with excitation energy equal to the binding energy of the emitted electron. The atom returns to the ground state by emitting fluorescence photons. The probabilities for a transition to lower energy subshells are extracted from the EADL library. The fluorescence photons are emitted isotropically.

### Bremsstrahlung

The total cross section at kinetic electron energy $T$ is calculated by eq. 2.1. The probability for the emission of a photon of kinetic energy $t$ is calculated from

$$P(T, t) = \frac{a(T)}{t} + b(T) \tag{2.6}$$

The coefficients $a$ and $b$ are obtained by fitting the energy distributions of the emitted photons at few $T$ values as they are available at the EEDL library. The values of the coefficients at different incident electron energies are calculated by interpolation. The direction of motion of the electron is not changed in the interaction. There are three models for the angular distribution of the emitted photons. In the present simulations, the Tsai cross section was used [22].

### Ionisation

In the case of ionisation, the total cross section for an incident electron of kinetic energy $T$ is calculated as the sum of the partial cross sections for all the subshells of an element. The partial cross sections are calculated by eq. 2.1 using the cross section data in the EEDL library. The partial cross sections are also used to select the shell from which the secondary electron will be emitted. The probability of emission of a $\delta$-ray with kinetic energy $t$ from a subshell of binding energy $B_i$ is given by

$$P(T, t, B_i) = \sum_{j=2}^{7} \frac{a_j(T)}{(t + B_i)^j} \tag{2.7}$$

for $T < T_0$ and

$$P(T, t, B_i) = \frac{c(T)}{t^2} \tag{2.8}$$

for $T > T_0$, where $T_0$ is a parameter. The coefficients in eqs. 2.7 and 2.8 are calculated by fitting EEDL data and their energy dependence is calculated by interpolating from the values resulting from the fits. The angles of emission of the primary and secondary electrons are calculated by energy and momentum conservation. The deexcitation of the atom proceeds as in the case of the photoelectric effect (fluorescence photons and Auger electrons).

# 3 RESULTS AND DISCUSSION

Measurements were done at SSD = 100 cm and 250 cm at stationary geometries. The diode measurements are presented in section 3.1. The ionisation chamber measurements were performed according to IAEA TRS-398 [23] and are described in section 3.2. The extraction of the energy spectrum of the beam is the subject of section 3.3. An overview of the simulations is given in section 3.4 and their results are presented in sections 3.5 - 3.8. In section 3.9, the simulated $R_{MC}$ is used to calculate the rotational absorbed dose at the prescription depth. A discussion on the properties of the simulation that need to be further investigated is given in section 3.10. The summary and conclusions of this study are presented in section 3.11. All measurements and simulations of the absorbed dose were performed along the central axis of the phantom.

## 3.1 Diode measurements

The percentage ionisation depth distributions were measured at SSD = 100 cm and 250 cm using a Scanditronix 60 x 60 x 60 cm³ water tank with Scanditronix Si-diode detectors. The diameter of the sensitive area of the field diode is 2.5 mm and the displacement of the effective point of measurement from the front of the detector is 0.4 mm. For each SSD, the ionisation as a function of depth was measured without and with the degrader plate.

The measured distributions are given in figure 3.1. The peak of the distribution moves to more shallow depths as the SSD increases due to the divergence of the beam and energy loss in air. The effect of the degrader is very pronounced at both SSD values.
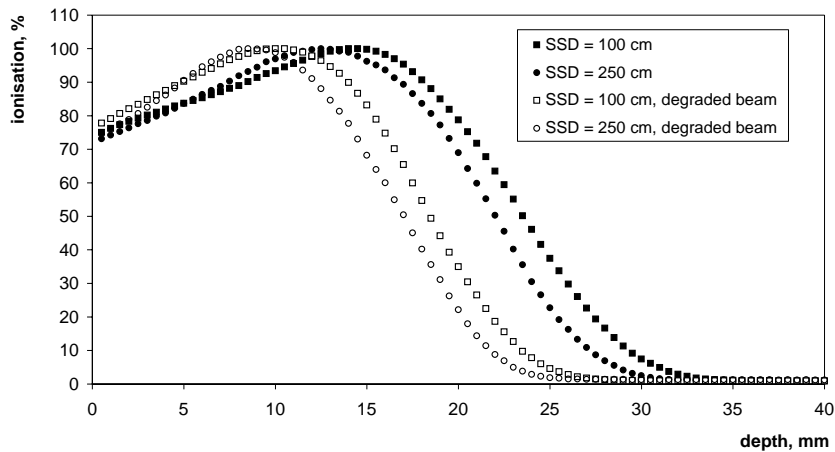


**Figure 3.1.** Ionisation depth measurements at SSD = 100 cm (squares) and 250 cm (circles). The closed (open) symbols show measurements without (with) degrader.

The ionisation depth distribution measurements were done for two reasons: (a) to derive the beam description in air at some distance between the accelerator head and the surface of the phantom and (b) to compare the measured distributions with the simulated ones as a cross-check of the simulation. In the latter case, the absorbed dose at a certain depth should also be measured with an ionisation chamber. In both cases, the ionisation depth distributions should in principle be converted to depth dose distributions, by taking into account the variation in the ratio of the collision stopping powers between

water and silicon, $S_{water,\,Si}$ as a function of depth $z$ ($S_{water,\,Si}(z)/S_{water,\,Si}(z_{max})$). An estimate of this correction is given below.

The mean energy of the beam at the phantom surface (in MeV) can be calculated as

$$\overline{E}_0 \;=\; 2.33R_{50} \tag{3.1}$$

where $R_{50}$ is the depth at which the dose is 50% of the maximum dose (in cm). These parameters are given in table 3.1.

| SSD, cm | $R_{50}$, cm | $\overline{E}_0$, MeV |
|---|---|---|
| 100 (w/o degrader) | 2.35 | 5.48 |
| 250 (w/o degrader) | 2.20 | 5.13 |
| 100 (with degrader) | 1.85 | 4.31 |
| 250 (with degrader) | 1.70 | 3.96 |

**Table 3.1:** $R_{50}$ and $\overline{E}_0$ values for the ionisation depth distributions in figure 3.1.

An estimate of the stopping power ratio water/silicon can be calculated if we assume that the most probable electron energy is $(E_p)_0 = 6$ MeV for the cases where no degrader plate is used and SSD = 100 cm. The practical range, $R_p$, of the beam can then be calculated from the relation [2, 24]

$$(E_p)_0(\text{MeV}) \;=\; 0.22 + 1.98R_p + 0.0025R_p^2$$

to be

$$R_p \;=\; 2.91 \text{ cm} \tag{3.2}$$

The mean energy of the beam at depth $z$, $\overline{E}_z$, can then be calculated as

$$\overline{E}_z \;=\; \overline{E}_0\!\left(1 - \frac{z}{R_p}\right) \tag{3.3}$$

and this value can be used to extract the water-silicon collision stopping power ratio from figure 3.2(a).

From figure 3.1, we see that $z_{max} = 1.45$ cm. From eqs. 3.1, 3.2 and 3.3, $\overline{E}_z$ was then calculated at $z_{max}$ and at $z = 0.1$ cm, 1 cm, 2 cm, 2.5 cm and 2.9 cm and the ratio

$$S_{water,\,Si}(z)/S_{water,\,Si}(z_{max})$$

was calculated from figure 3.2(a). The results are given in figure 3.2(b). The figure shows that the correction becomes 5% at about 2.5 cm depth, where the dose is approximately 40% of the peak value. Given that $(E_p)_0$ is not known before the beam spectrum is calculated and that the beam characterization is done under a number of approximations (e.g. the 0.5 mm correction for the diode effective point of measurement and phantom window were not taken into account when the beam analysis was done), the stopping power correction was neglected and the ionisation measurements was used directly as depth dose measurements.
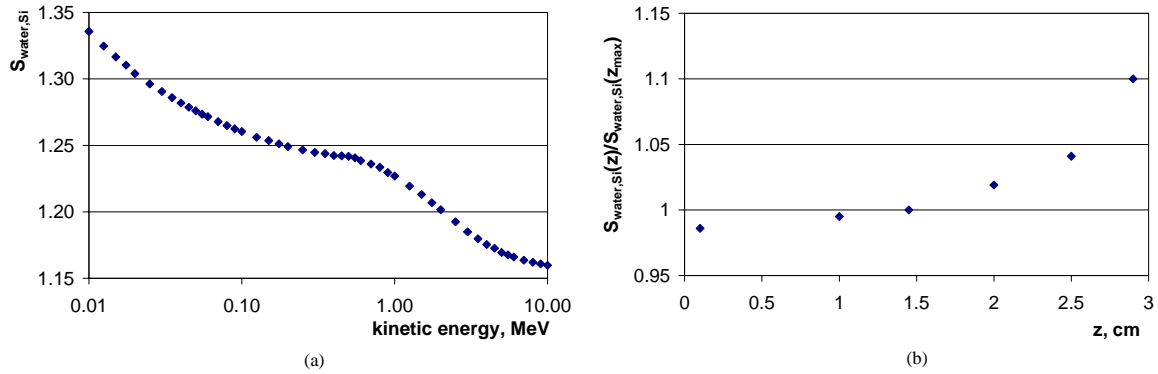
**Figure 3.2.** (a) Variation of the ratio of the collision stopping powers in water and silicon as a function of the electron kinetic energy [25], (b) Correction factor for the ratio of collision stopping powers between water and silicon as a function of depth.

## 3.2 Ionisation chamber measurements

In order to normalize the simulation, the absorbed dose has to be measured at a given depth so that the number of monitor units (MU) in the measurement will be related to the number of primary electrons in the simulation. This measurement was done at SSD = 100 cm and SSD = 250 cm (and for both beam energies) in a stationary geometry.

Absorbed dose measurements were done according to [23] using a NACP02 plane-parallel chamber at 1 cm depth in a RMI solid water phantom. The electrometer was of Farmer 2570 type. Measurements were done at $V_1 = 249.5$ V and $V_1 = 62$ V to calculate the recombination correction. The polarity correction was neglected. The beam quality factors were calculated for the $R_{50}$ values in table 3.1. The ionisation chamber was placed at 1 cm depth in the phantom

$$z_{ph} = (1 \text{cm})\rho_{ph} = 1.03 \text{ g} \cdot \text{cm}^{-2}$$

The water-equivalent depth is

$$z_w = z_{ph} \cdot c_{ph} = 0.98 \text{ g} \cdot \text{cm}^{-2}$$

where $c_{ph} = 0.949$ is the depth-scaling factor for the material of the phantom. The ionisation chamber has a wall of mylar whose thickness is 0.6 mm or 0.104 gcm-2 which multiplied by an approximate depth-scaling factor of 0.9 gives a total water-equivalent depth of

$$z_w = 1.07 \text{ cm}$$

The electrometer reading has also to be scaled as

$$M_Q = M_{Q, ph} \cdot h_{ph}$$

where $h_{ph} = 1.008$ is the fluence scaling factor for the phantom. The absorbed dose was calculated according to

$$D_{w, Q} = M_Q \cdot k_s \cdot k_{elec} \cdot k_{TP} \cdot N_{D, W} \cdot k_Q \quad (3.4)$$

The details of the calculation are shown in table 3.2. The chamber was calibrated in a cobalt beam, so the expected combined standard uncertainty in absorbed dose calculation under reference conditions is about 2% [23]. The deviations from the reference conditions in the measurements (large field, large SSD,

plastic phantom, approximations in the calculations) entail an additional uncertainty, which, however, has not been estimated.

| | SSD = 100 cm w/o degrader | SSD = 100 cm with degrader | SSD = 250 cm w/o degrader | SSD = 250 cm with degrader |
|---|---|---|---|---|
| $k_s$ | 1.0107 | 1.0095 | 1.0022 | 1.0017 |
| $k_{elec}$ | 1.0031 | | | |
| $k_{TP}$ | 1.0057 | | 1.0078 | |
| $N_{D,W}$, mGy/nC | 157.3 | | | |
| $k_Q$ | 0.926 | 0.934 | 0.928 | 0.937 |
| $D_{w,Q}$, Gy/MU | 0.027 | 0.025 | 0.0043 | 0.0022 |

**Table 3.2:** Calculation of absorbed dose to water for SSD = 100 cm and SSD = 250 cm for the nominal and for the degraded beam.

The absorbed dose distributions as a function of depth are given in figure 3.3. In [8], the absorbed dose was measured at SSD = 250 cm with a 5 mm polystyrene degrader to be 0.00178 Gy/MU at 7 mm water-equivalent depth, which can be compared to the value 0.0022 Gy/MU in the present measurement.
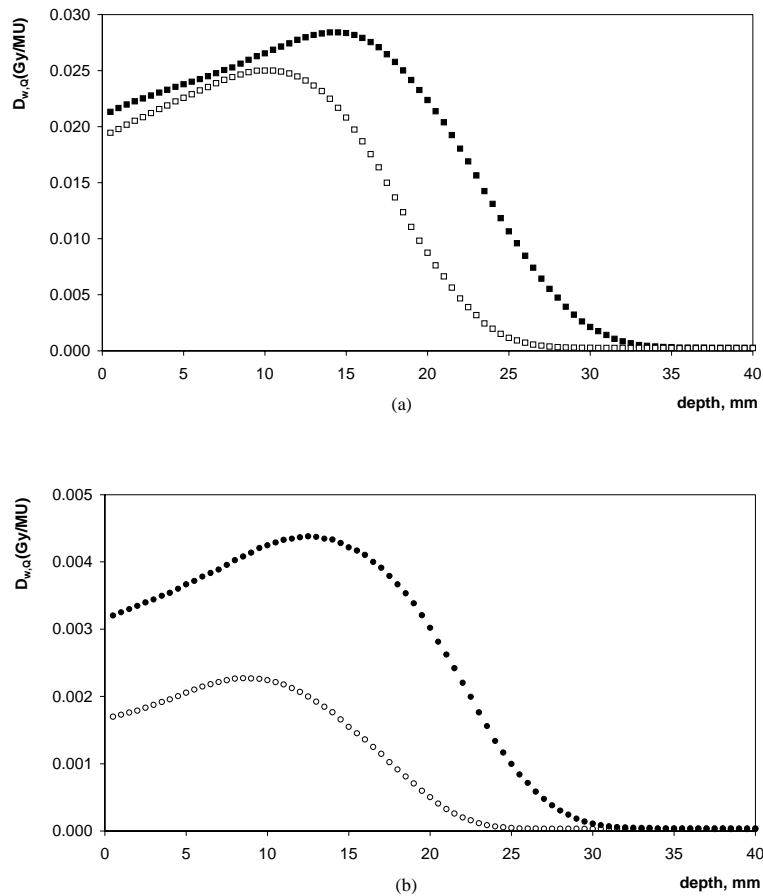


**Figure 3.3.** Absorbed dose distributions at (a) SSD = 100 cm and (b) SSD = 250 cm. The closed (open) symbols show measurements without (with) degrader.

## 3.3 Calculation of the energy spectrum

The beam characterization, which is used as starting point in the Geant4 calculations, was derived [11] using the coupled multi-source electron beam phase space model implemented in the OTP treatment planning system (VMC++) [26] as follows.

Let $F(E)$ be the fluence distribution in energy at the exit phase space plane of the accelerator, with $E$ denoting the kinetic energy of the primary electron. If the depth dose of a monoenergetic broad beam in water is $D_{mono}(E, z)$ and the photon background is $D_{\gamma}(z)$, the depth dose curve for the accelerator can be calculated as

$$D(z) = D_{\gamma}(z) + \int F(E)D_{mono}(E, z)dE \qquad (3.5)$$

The function $F(E)$ is parametrized as a mathematical function with a number of unknown constants. The energy spectrum $F(E)$ is then extracted from eq. 3.5 by using a large number of precalculated distributions $D_{mono}(E, z)$ in a given energy interval and minimizing the difference $(D_{meas}(z) - D(z))^2$. Gauss-Legendre quadrature is used to calculate the integration in eq. 3.5. The precalculation of the depth dose curves is done for a grid of energies and the depth dose distribution at an arbitrary energy is then calculated by linear interpolation between the calculated curves. The density of the grid is chosen so that the accuracy of the interpolated curves be better than 0.2% (i.e. 0.25 MeV at energies below 2 MeV, 0.5 MeV in the range 2-5 MeV and 1 MeV above 5 MeV). In the present calculation, the function $F(E)$ was given by the sum of two Woods-Saxon functions and a linear term for the low energy tail of the distribution. The measured ionisation-depth distribution at SSD = 100 cm without degrader was used as $D_{meas}(z)$. Only depths greater than 4 mm were used in the fit to neglect low energy electrons that deposit their energy close to the surface of the phantom. The measured and fitted percentage depth dose distributions are shown in figure 3.4(a). The resulting energy probability density function, $F(E)$, is shown in figure 3.4(b). The most probable value in the distribution is 5.94 MeV and the mean value is 5.78 MeV. The energy spectrum was derived from the aforementioned characterization of a 6 MeV Clinac 2100C/D OTP electron beam. In the Geant4 simulations, this probability density distribution was integrated at initialization time and the cumulative probability distribution was then used to sample the kinetic energy of the primary electrons by uniformly generating random numbers in the interval (0, 1). The reproduced energy distribution of primary electrons in Geant4 is also shown in figure 3.4(b) as a cross-check.
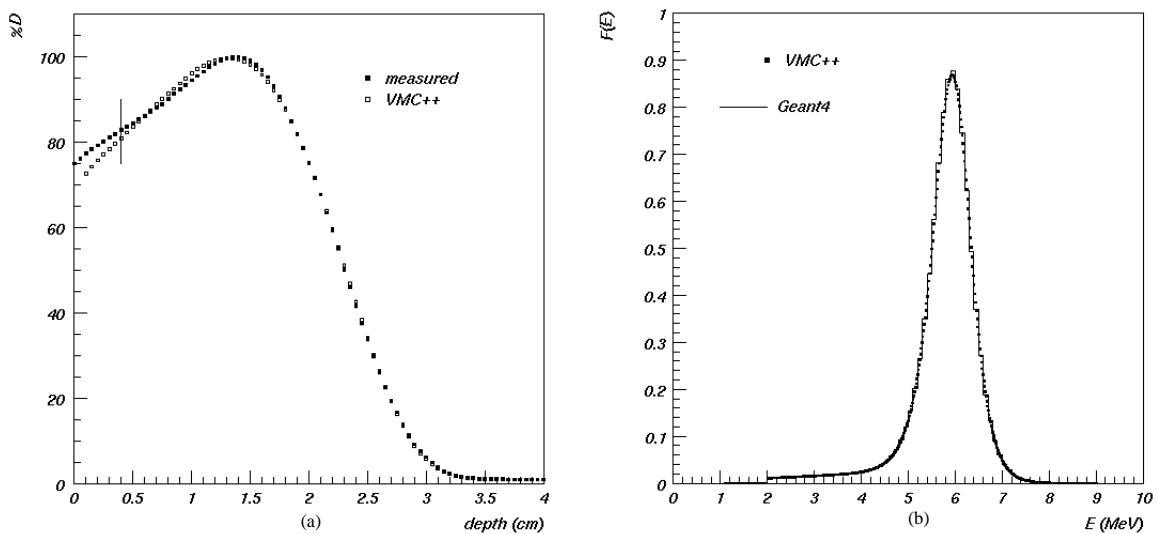


**Figure 3.4.** (a) Measured (closed squares) and fitted in VMC++ (open squares) percentage depth dose distributions at SSD=100 cm without degrader. (b) Kinetic energy distribution for the primary electrons as was fitted in VMC++ (squares) and reproduced by Geant4 (histogram).

## 3.4   Overview of the simulations

The simulations were scoring energy depositions along the main axis (x) of the water phantom within a cylinder of radius *r*. As there were no voxels used in the geometry, the program calculated first the fraction of the energy deposition within the scoring cylinder and then the energy deposition for each bin in the depth dose distribution. The binning of this distribution was 0.5 mm. The geometry occasionally entailed approximate calculations of the masses in the first 2-4 bins in the distribution by numerical integration [27]. In all runs, the incidence angle of the beam was between $0°$ and $90°$ (eq. 1.5).

The simulation runs were done with varying radius, *r,* and step, $\Delta\vartheta$, in the beam incidence angle, different phantom geometries and physics models. For convenience, an overview of the simulation runs is given in this section, listing their parameters. The results of the simulations are given in the sections that follow.

In order to compare the simulation physics models with the measurements, the following simulation runs were first done in a stationary geometry:

- SSD = 100 cm, *r* = 2 cm, cubic phantom (50 cm side), standard em physics
- SSD = 100 cm, *r* = 2 cm, cubic phantom (50 cm side), low-energy em physics
- SSD = 250 cm, *r* = 2 cm, cubic phantom (50 cm side), low-energy em physics

The results of these runs are given in section 3.5. The conclusion was that the low-energy model should be used in the rest of the runs.

As the scoring volume radius, $r$, and the beam incidence angle step, $\Delta\vartheta$, were arbitrary parameters in the simulations, three test runs were done in order to have an estimate of their effect on the calculations. The test runs had the following parameters:

- test run 1: SSD = 250 cm, *r* = 2 cm, $\Delta\vartheta = 10°$, elliptic phantom (35 cm x 50 cm)
- test run 2: SSD = 250 cm, *r* = 0.5 cm, $\Delta\vartheta = 10°$, elliptic phantom (35 cm x 50 cm)
- test run 3: SSD = 250 cm, *r* = 0.5 cm, $\Delta\vartheta = 5°$, elliptic phantom (35 cm x 50 cm)

The cross-sectional dimensions of the phantom in the test runs were somewhat overestimated (35 cm x-axis and 50 cm z-axis) as one extreme case so as to have an estimate of how many primary electrons are needed to be simulated so that all simulations would give a statistical accuracy of $R_{MC}$ of about 2%. The height of the phantom was set to 25 cm (this value was used in subsequent runs as well). The results of the test runs are given in section 3.6. The conclusion was that it is sufficient to use the following parameters in the simulation:

- a scoring volume radius, *r*, of 2 cm,
- a step $\Delta\vartheta = 10°$ in angle of incidence,
- 10 million events per angle for $\vartheta > 0°$ and
- 40 million events for $\vartheta = 0°$.

The above parameters were then used to simulate the depth dose distributions with varying phantom dimensions which resemble the patient anatomy. The following runs were performed:

- SSD = 250 cm, elliptic phantom 20 cm x 40 cm
- SSD = 250 cm, cylindrical phantom with 30 cm diameter

The results of these runs are given in section 3.7. In all phantom geometries, a high surface dose was observed for the rotational geometry. All simulations above assumed a production threshold of 10 keV for photons and 100 keV for electrons in water. To see if the high surface dose is an effect of the

production thresholds, the cut for electron production was reduced to 10 keV and the calculations for the cylindrical phantom were repeated. The results of this calculation are discussed in section 3.8.

## 3.5   Comparison between measurement and simulation at stationary geometries

In order to select the physics model, a comparison was made between the measured depth dose distribution at SSD = 100 cm (without degrader) and the calculated depth dose distributions using the cubic phantom (section 2.2) and the two Geant4 models for electromagnetic physics (section 2.4).

In order to compare the calculated depth dose distributions to the measured one, the measured values were first linearly interpolated to the center of the bins used in the simulations. The value of the first bin in the resulting histogram was calculated using the first two measured values. The simulated distributions were normalized to the absorbed dose measurement in table 3.2, i.e. at bin 22 (covering depths from 10.5 mm to 11 mm) (this was taken to be bin 21 in the simulated distribution to take into account the 0.5 mm shift in depth that was neglected in the beam analysis). The comparison between the normalized Monte Carlo distributions and the measurement (figure 3.5(a)) seemed to favour the low-energy model, which was therefore used in subsequent calculations. The same procedure as described above was used to normalize the simulated depth dose distribution at SSD = 250 cm. The comparison with the measurement is shown in figure 3.5(b).

Figure 3.5 shows that the simulation can reproduce the shape of the dose distributions rather well. The discrepancy between measurement and calculation for the low-energy model near the surface in figure 3.5(a) is due to the fact that the simulation took into account only direct electrons. On the other hand, the simulation seems to overestimate the dose close to the surface at SSD = 250 cm.
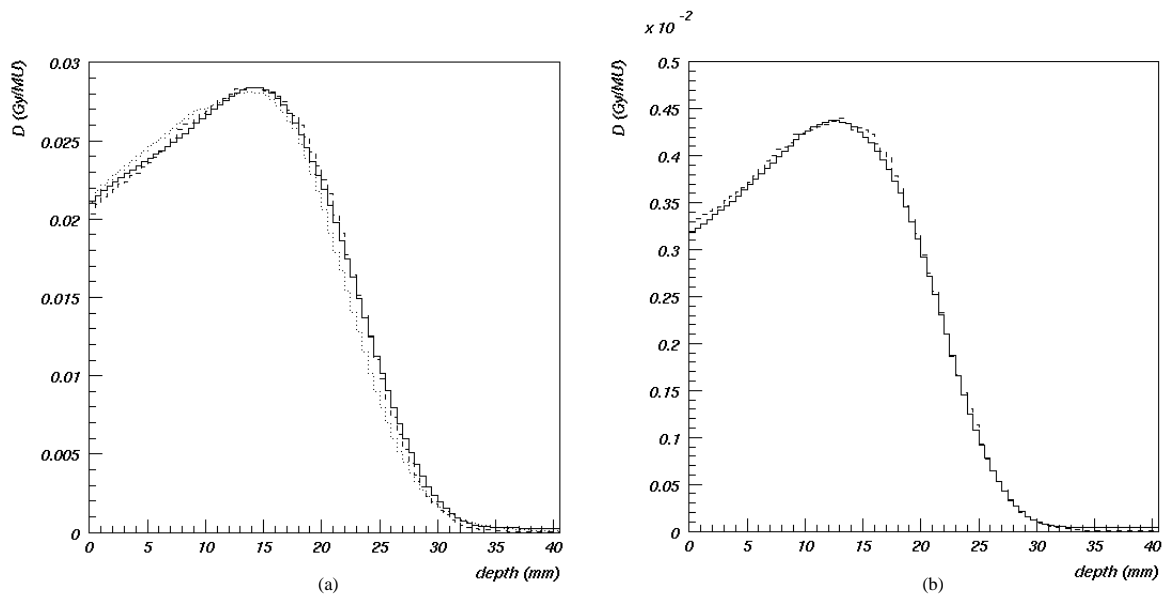


**Figure 3.5.**   (a) Comparison between the measured (solid line) and simulated absorbed dose distribution at SSD = 100 cm for two physics models: the standard electromagnetic model (dotted line) and the low-energy electromagnetic model (dashed line). (b) Comparison between the measured (solid line) and simulated (dashed line) absorbed dose distribution at SSD = 250 cm.

## 3.6   Test simulations

The number of primary electrons was initially set to $10^7$ per angle and $10^8$ per angle for the cases where $r = 2$ cm and $r = 0.5$ cm, respectively. The aim was to have an estimate of the number of primary electrons required to calculate the ratio $R_{MC}$ with a given statistical uncertainty, which was taken to be 2% (by 'statistical uncertainty' is meant one standard deviation of all energy depositions in one bin).

The depth dose distributions for various $\vartheta$ values in test run 1 are given in figures 3.6 - 3.7(a). The distributions are normalized to the number of events. The depth dose distribution at $\vartheta = 0°$ shows how the electromagnetic shower of particles develops along the beam direction. At nonzero angles, the shower starts developing outside the scoring volume and when it reaches the central phantom axis it is at a 'later' stage compared to the $\vartheta = 0°$ case. This explains why the depth dose distributions at $\vartheta > 0°$ seem to 'shift' to shallower depths as $\vartheta$ increases. Figure 3.7(a) shows that the depth dose distributions at $\vartheta = 70°$ and $\vartheta = 80°$ have very pronounced peaks at the surface of the phantom.

The percentage depth dose distributions in figures 3.6 - 3.7(a) were added according to eq. 1.5 to calculate the depth dose distribution for one rotation. The resulting distribution is given in figure 3.7(b) (dashed line), where the depth dose distribution at $\vartheta = 0°$ (solid line) is also plotted for comparison. The rotational depth dose distribution has no build-up region, as expected [5], but the surface dose seems to be overestimated. This may be due to the fact that the production cuts were too high to accurately describe the interactions of electrons near the surface of the phantom when the angle of incidence of the beam is high.
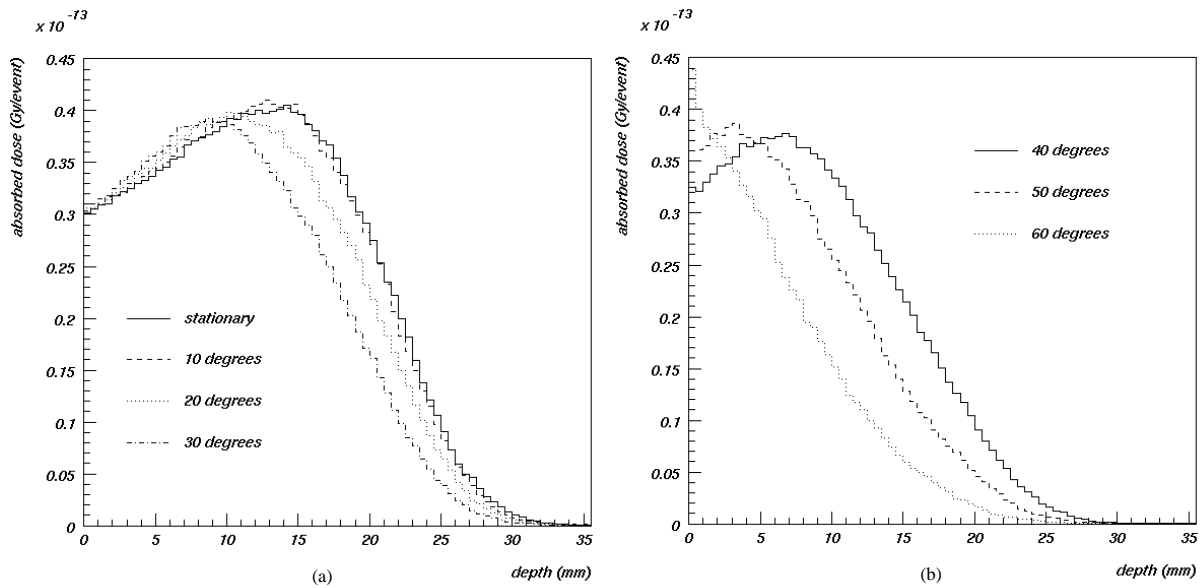


**Figure 3.6.**   Results of test run 1: (a) depth dose distributions for $\vartheta = 0°$ (solid line), $\vartheta = 10°$ (dashed line), $\vartheta = 20°$ (dotted line) and $\vartheta = 30°$ (dashed-dotted line). (b) depth dose distributions for $\vartheta = 40°$ (solid line), $\vartheta = 50°$ (dashed line) and $\vartheta = 60°$ (dotted line). The distributions are normalized to the number of events ($10^7$ per angle).
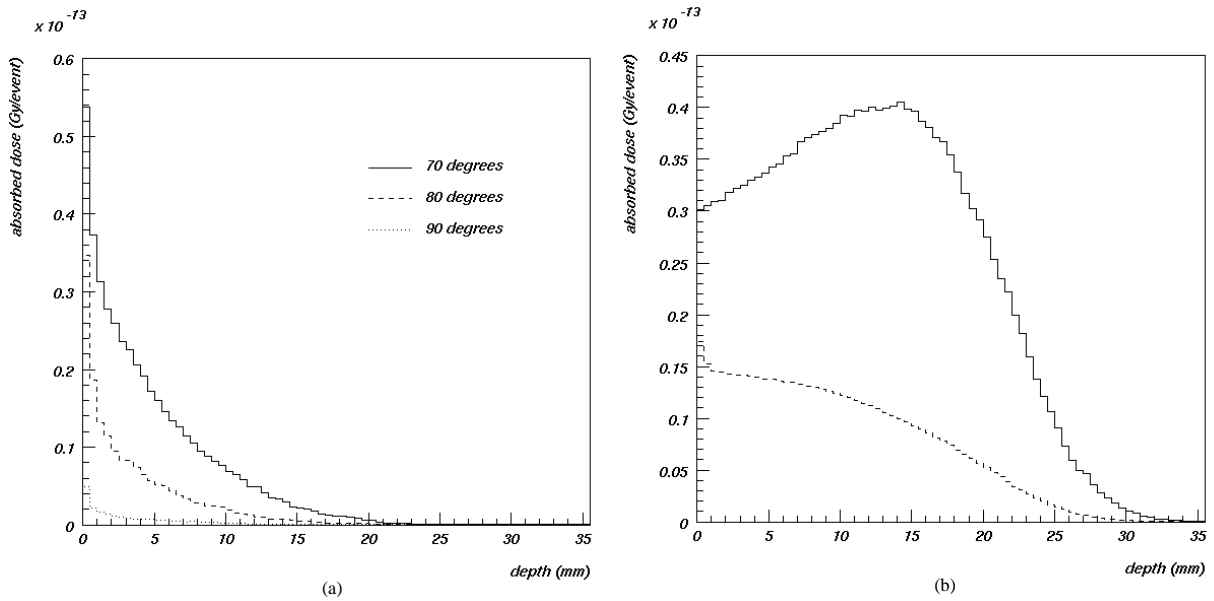
**Figure 3.7.** Results of test run 1: (a) Depth dose distributions for $\vartheta = 70°$ (solid line), $\vartheta = 80°$ (dashed line) and $\vartheta = 90°$ (dotted line). The distributions are normalized to the number of events ($10^7$ per angle). (b) Depth dose distributions for $\vartheta = 0°$ (solid line) and for one rotation (dashed line).

The $R_{MC}$ distribution for test run 1 was calculated according to eq. 1.8 and is given in figure 3.8(a). It has an almost linear dependence with depth starting at about 0.65 at the surface and becoming unity at 7 mm depth approximately. The statistical uncertainty of the calculation is shown in figure 3.8(b). As the figure shows, its main contribution stems from the uncertainty in the stationary depth dose distribution. To reduce the statistical uncertainty of $R_{MC}$ by a factor 2, the number of primary electrons generated for $\vartheta = 0°$ was increased by a factor 4.
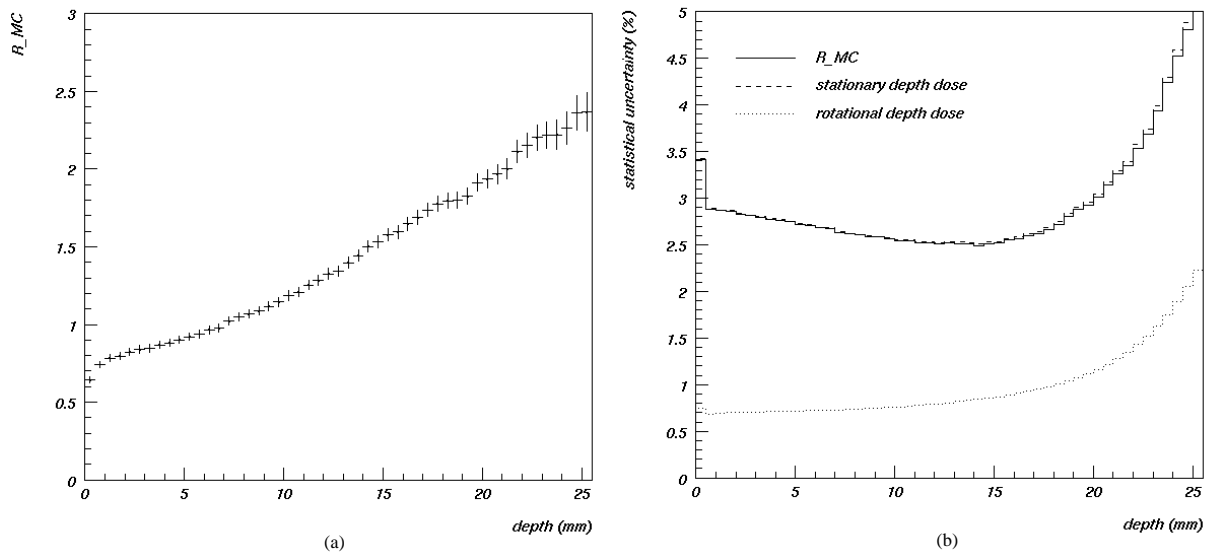


**Figure 3.8.** Results of test run 1: (a) $R_{MC}$ with statistical uncertainty ($10^7$ events per angle). (b) Relative statistical uncertainty (one standard deviation) for: $R_{MC}$ (solid line), the stationary depth dose distribution (dashed line) and the depth dose distribution for one rotation (dotted line).

The statistical uncertainty of the $R_{MC}$ calculation for the test runs 2 and 3 was similarly dominated by the uncertainty of the stationary depth dose distribution, and was of the same order as in run 1. The statistics was, therefore, increased by a factor 4 for the electrons which were generated at $\vartheta = 0°$ in order to reduce the statistical uncertainty to about 2%.

The calculations for the increased statistics at $\vartheta = 0°$ are given in figures 3.9 - 3.11. Figure 3.9(a) shows the depth dose distributions at $\vartheta = 0°$ for the two radii of the scoring cylinder. The absorbed dose seems to be lower in the 0.5 cm radius case and up to a depth of 15 mm but the difference is within statistical uncertainty, as shown in figure 3.9(b). The depth dose distributions for the three test runs for one rotation is shown in figure 3.10(a). The trend of decreased energy deposition in the case of the 0.5 cm radius is present here also but the discrepancy is now statistically significant, as shown in figure 3.10(b). On the other hand, the angle step does not seem to have any effect on the calculation. The calculated $R_{MC}$ values are shown in figure 3.11(a). The distributions are identical up to 15 mm depth. From 15 mm to 25 mm, the 0.5 cm radius calculation seems to give slightly higher $R_{MC}$ values. The difference between the $R_{MC}$ calculations in run1 and run 3 is shown in figure 3.11. The statistics is too low to determine the values of $R_{MC}$ at depths greater than 25 mm.
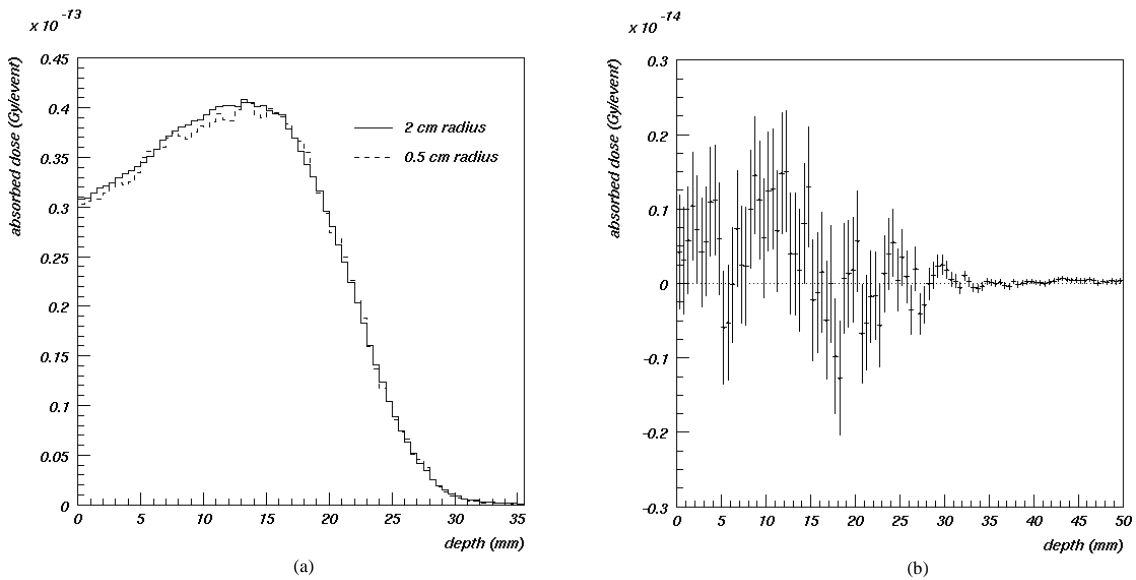


**Figure 3.9.** Results of test runs 1 - 3 with increased statistics at $\vartheta = 0°$: (a) Stationary depth dose distributions for 2 cm radius (run 1) and for 0.5 cm radius (runs 2 and 3). (b) Difference of stationary depth dose distributions for 2 cm radius and 0.5 cm radius. The uncertainty is statistical.
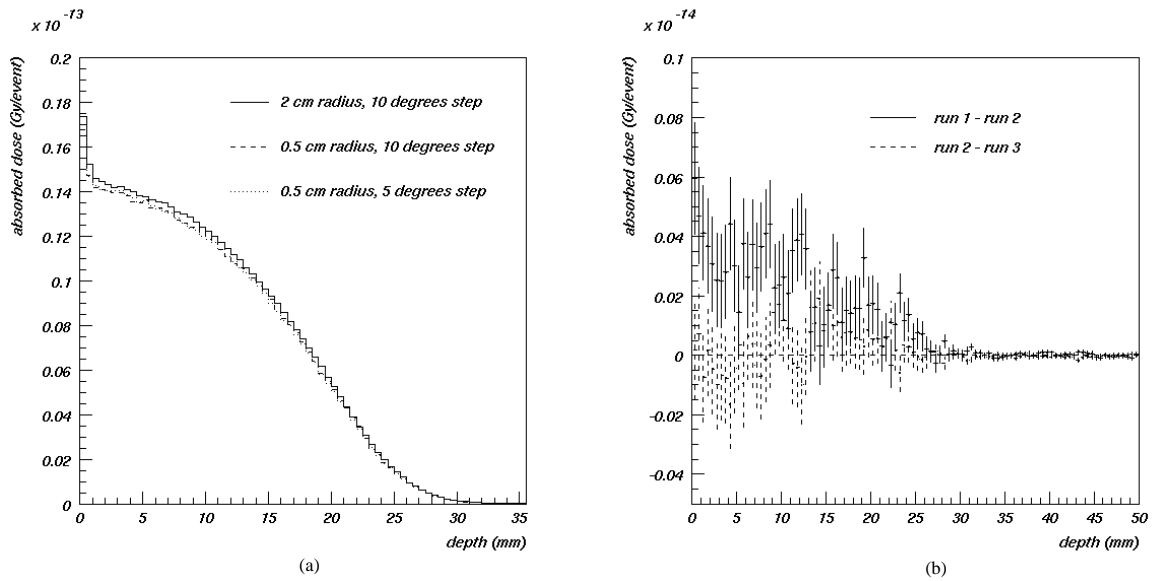
**Figure 3.10.** Results of test runs 1 - 3 with increased statistics at $\vartheta = 0°$: (a) Depth dose distribution for one rotation in run 1 (solid line), run 2 (dashed line) and run 3 (dotted line). (b) Difference between the runs in the depth dose distributions for one rotation. The solid crosses show the difference between run 1 and run 2 (change in radius of scoring volume). The dashed crosses show the difference between run2 and run 3 (change in angle step).
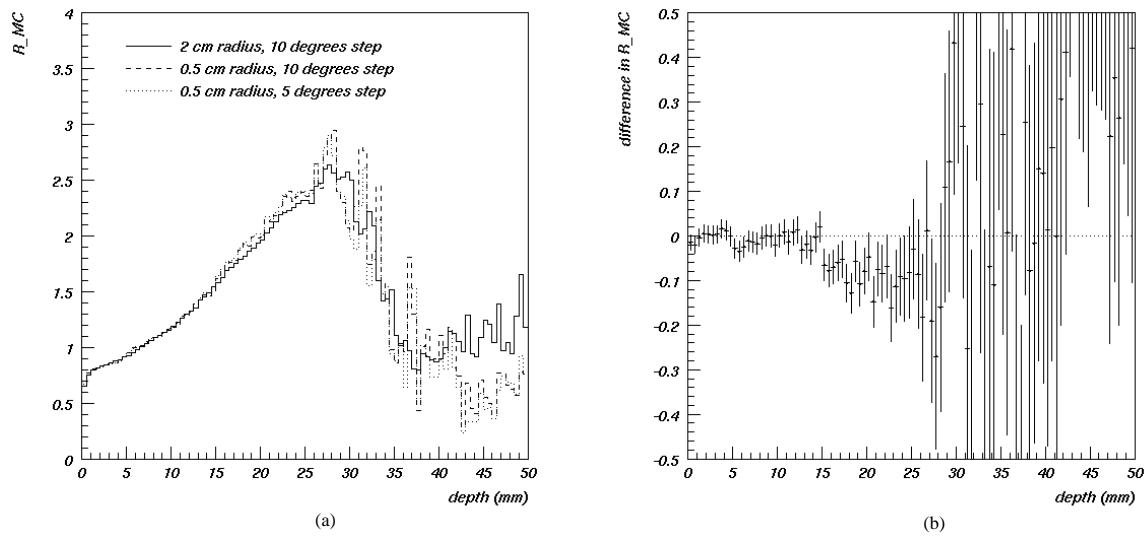


**Figure 3.11.** Results of test runs 1 - 3 with increased statistics at $\vartheta = 0°$: (a) $R_{MC}$ calculation for run 1 (solid line), run 2 (dashed line) and run 3 (dotted line). (b) Difference in $R_{MC}$ between run 1 and run 3.

The conclusion from the test runs above is that it is sufficient to use the following parameters in the simulation:

- a scoring volume radius of 2 cm,
- a step $\Delta\vartheta = 10°$ in angle of incidence,
- 10 million events per angle for $\vartheta > 0°$ and
- 40 million events for $\vartheta = 0°$.

Using the parameters above, more realistic phantom dimensions were subsequently used to calculate the stationary and rotational depth dose distributions and their ratio, $R_{MC}$. These runs are discussed in the following two sections.

## 3.7 Calculations for varying phantom cross-sections

As a first approach to simulating realistic patient dimensions, the depth dose distributions were calculated at SSD = 250 cm for an elliptic phantom with the following x- and z-axis dimensions:

- 20 cm x 40 cm
- 30 cm x 30 cm (phantom used for the measurements in [8])

The height of the phantom was the same as in the test runs (25 cm). The stationary and rotational distributions for these runs are given in figure 3.12, whereas the resulting $R_{MC}$ distributions are shown in figure 3.13. The distributions for test run 1 are also shown for comparison. The plots show that all distributions have a dependence on the dimensions of the phantom, which is most clearly seen between the distributions of the test run and the distributions of the more realistic phantoms.
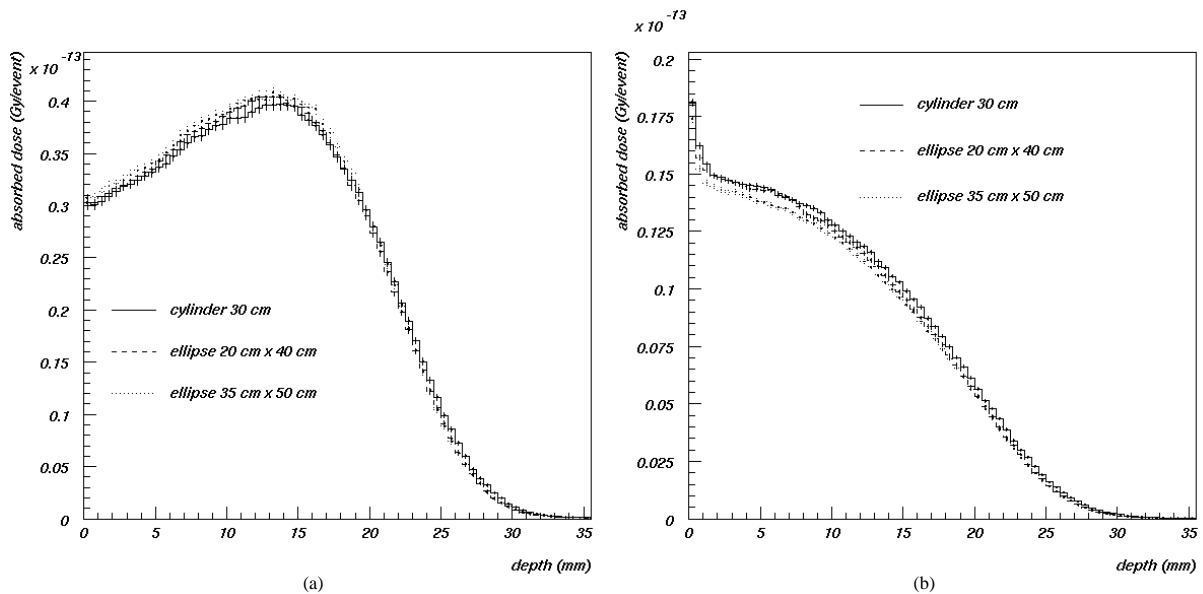


**Figure 3.12.** (a) Stationary and (b) rotational depth dose distributions for an elliptic phantom with a cross-section of 20 cm x 40 cm and for a cylindrical phantom of 30 cm in diameter. The distributions for the test run 1 (ellipse 35 cm x 50 cm) are also shown for comparison
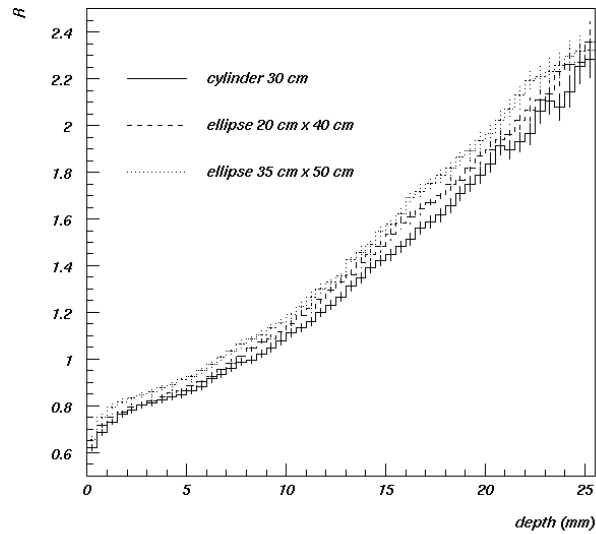
**Figure 3.13.** Calculation of $R_{MC}$ for an elliptic phantom with a cross-section of 20 cm x 40 cm and for a cylindrical phantom of 30 cm in diameter. The distribution of $R_{MC}$ for the test run 1 (ellipse 35 cm x 50 cm) are also shown for comparison.

## 3.8 Reducing the production thresholds

The high surface dose of the calculated rotational depth dose distributions shown in figures 3.10(a) and 3.12(b) may be due to high production cuts in the simulation. The highest production threshold in the calculations discussed thus far is the threshold for secondary electron production in water (100 keV). To check whether this cut is responsible for the high surface dose, the calculations for the cylindrical phantom were repeated with the addition of an inner phantom covering the region of energy scoring.

The geometry is shown in figure 3.14. The inner phantom was defined as a cylindrical section of 15 cm outer radius, 11 cm inner radius, 4 cm height and covering an angle of 30° symmetrically placed about the x-axis of the outer phantom. In the inner phantom, the production threshold for the secondary electrons was set to 10 keV. The production thresholds in the outer phantom were as in the previous simulations.
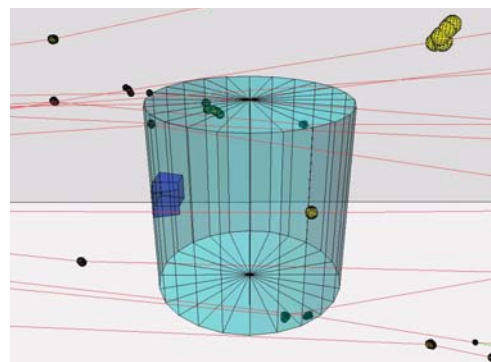


**Figure 3.14.** Cylindrical geometry with an inner phantom placed around the x-axis to cover the region where energy is scored.

The depth dose distribution for one rotation and the $R_{MC}$ distribution are shown in figure 3.15, where they are compared with the calculation shown in figures 3.12 and 3.13 (cylindrical phantom with uniform cuts). The figure shows that reducing the electron production cut from 100 to 10 keV removes most of the excess in surface dose. The dose value in the first bin still seems to be somewhat high but this may be due to the dimensions of the inner phantom. The rotational depth dose distribution does not seem to be significantly affected by the change in cuts after 5 mm depth but the $R_{MC}$ distributions differ

up to 15 mm depth. To see up to which depth the low production cut affects the calculation, the depth dose distributions per angle are compared for the cases with and without the inner phantom in figure 3.16. There is a considerable difference in the distributions at high angles and close to the surface of the phantom.
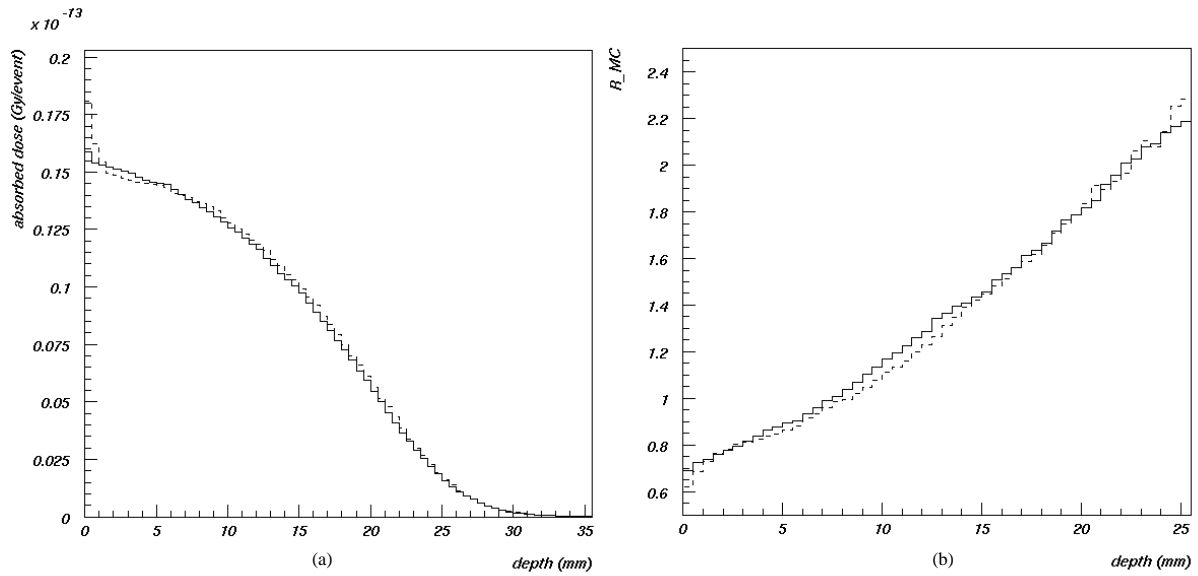


**Figure 3.15.** (a) Depth dose distributions for one rotation and (b) $R_{MC}$ distributions for the cylindrical phantom with (solid lines) and without (dashed lines) the inner phantom.
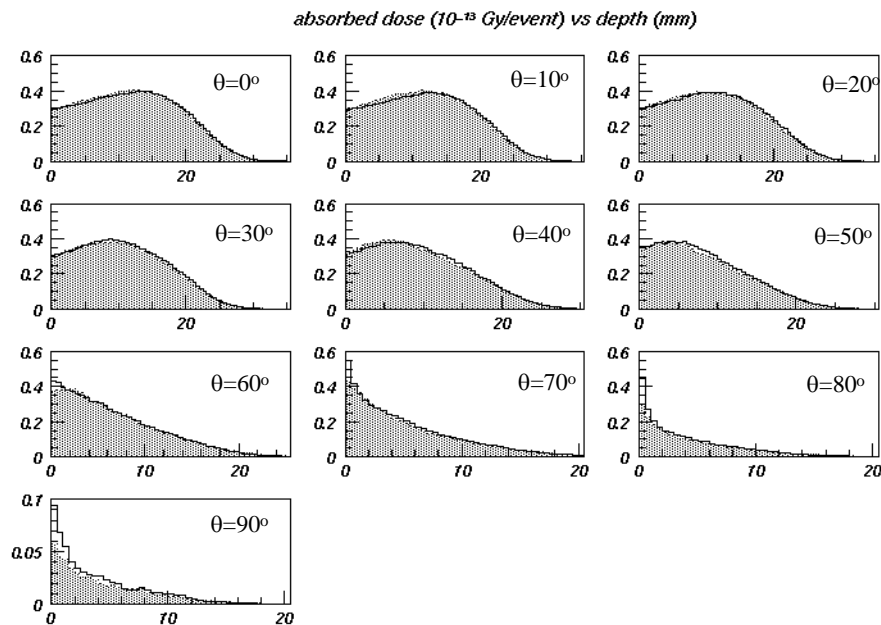


**Figure 3.16.** Depth dose distributions for various beam angles for uniform cuts (solid lines) and for low cuts in the inner phantom (filled histograms).

### 3.9    Absorbed dose at the prescription depth

At UMAS, patients are normally treated three times a week with a fraction dose of 2 Gy. The prescribed dose is 30 Gy for curative treatments and 20 Gy for palliative treatments. The prescription depth is 5 mm [8].

The low-threshold calculation for the cylindrical phantom discussed in the previous section gives the following value of $R_{MC}$ at 5 mm:

$$R_{MC}(5 \text{ mm}) = 0.88 \tag{3.6}$$

That value can be used to calculate the absorbed dose delivered in one rotation. The dose rate at the stationary geometry at SSD = 250 cm without degrader was measured to be 0.43 Gy/100 MU at 1.07 cm depth (table 3.2). From figure 3.1, this gives a dose rate of (83.696/98.281)*0.43 Gy/100 MU = 0.37 Gy/100 MU at 5 mm depth. From the definition of $R$ (eq. 1.1) and from eq. 3.6, we then obtain

$$\text{dose in one rotation (without degrader)} = \frac{0.37 \text{ Gy}}{0.88} = 0.42 \text{ Gy} \tag{3.7}$$

It follows that 2 Gy will be delivered in 5 rotations i.e. a treatment time of 1.5 minutes (since the number of rotations has to be an integer, their number may need to be varied between fractions so that the total dose will be as prescribed).

Assuming that $R_{MC}$ has the same value for the degraded beam also, the same calculation would give

$$\text{dose in one rotation (with degrader)} = \frac{0.20 \text{ Gy}}{0.88} = 0.23 \text{ Gy} \tag{3.8}$$

and 2 Gy would require 9 rotations, i.e. a treatment time of 2.7 minutes.

In the previous UMAS study [8], measurements of $R$ were performed for a different accelerator and only for the degraded beam. The assumption is made that these differences still allow a comparison between the measurements in [8] and the present simulations. The simulated $R_{MC}$ value at the surface of the phantom was 0.69 (cylindrical phantom, low cuts). It is found to be in the same interval as the values in [8], which ranged from 0.65 to 0.97.

### 3.10    Production cut dependence

To see how the SSD = 100 cm calculations are affected by a reduction in the electron production cut, the stationary depth dose distribution at SSD = 100 cm was recalculated for the same geometry as before (cubic phantom of 50 cm side) with the addition of an inner cube of 4 cm side, where the production cut for the electrons was set to 10 keV. The resulting distribution is shown by the dotted line in figure 3.17a, where the distribution for the 100 keV calculation (dashed line) and the measurement (solid line) are also shown. The 10 keV curve is normalized to the measured distribution at 1 cm depth. The relative difference between the measurement and the simulation is given in figure 3.17b.

The two Geant4 calculations are compared with the VMC++ calculation [11] of the percentage depth dose distribution in figure 3.18. Figures 3.17 and 3.18 show that the low-cut distributions seem to have a better overall agreement with the measurement and VMC++. This may be due to the fact that the simulations discussed in this report were run without setting a maximum allowed step length. Setting such a parameter might give an effect in the calculation, as the tracking of the electrons is done without taking into account the scoring grid dimensions.
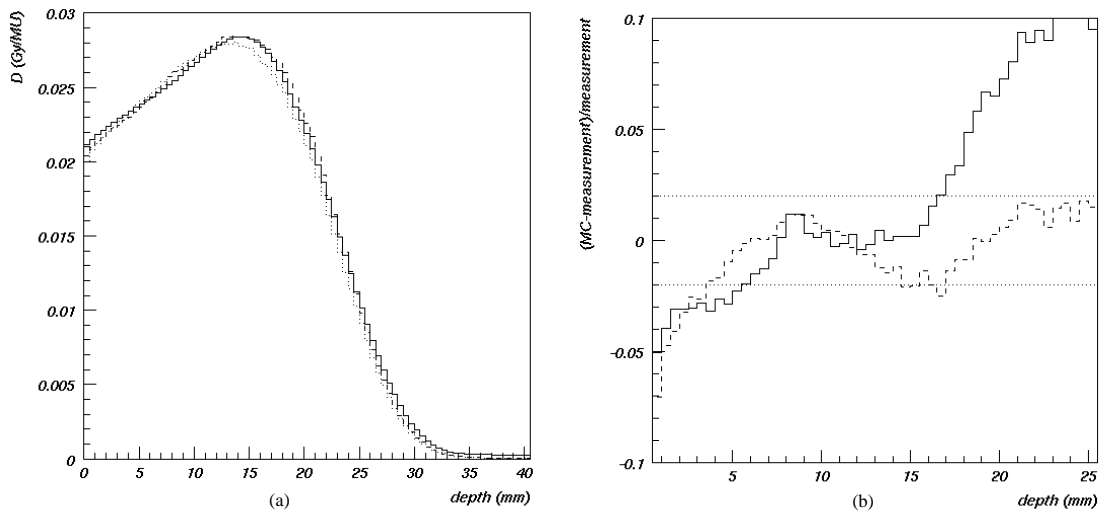
**Figure 3.17.** Depth dose distributions for SSD = 100 cm. (a) Solid line: measurement, dashed line: 100 keV calculation, dotted line: 10 keV calculation. (b) Relative difference between the simulated and measured distributions for the 100 keV calculation (solid line) and the 10 keV calculation (dashed line).
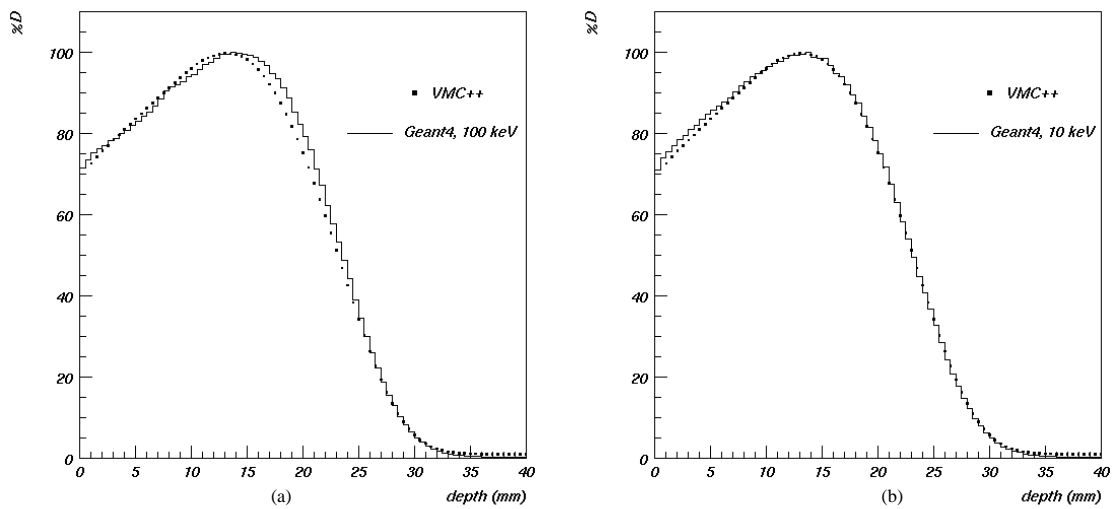


**Figure 3.18.** Comparison between VMC++ and Geant4 for (a) the 100 keV calculation and (b) the 10 keV calculation of the percentage depth dose distribution (SSD = 100 cm).

## 3.11 Summary

The study presented in this report is a first effort towards the calculation of absorbed dose distributions for treatment verification in total skin electron irradiation. Two Monte Carlo programs have been used in the study: Geant4 and VMC++. The aim of this study was to use Geant4 calculations to

relate the depth dose distributions in the stationary and rotational geometries. The study was conducted as follows.

Percentage depth dose and ionisation chamber measurements along the central beam axis were performed at SSD = 100 cm and 250 cm (treatment distance) for the nominal and for the degraded beam. The percentage depth dose distribution that was measured at SSD = 100 cm was used to extract the energy spectrum by fitting percentage depth dose distributions calculated by VMC++. This was done under a number of approximations regarding the accelerator geometry, field size, the virtual source position and the correction for the scattering of the electrons in the accelerator. Moreover, only direct electrons were considered.

Geant4 calculations were then done using two physics models, the standard electromagnetic and the low-energy electromagnetic, to simulate the depth dose distribution at SSD = 100 cm. The low-energy model seemed to describe the measurement best. The measured and simulated stationary depth doses distributions at SSD = 250 cm were also compared for the low-energy model and the simulation seemed to reproduce the measurement fairly well. The low-energy model was used in the rest of the simulations.

A set of simulations using that model were performed at the treatment distance (SSD = 250 cm) using a set of production thresholds for the secondary particles and phantom geometries (10 keV photon cut and 100 keV electron cut).

First, an elliptical phantom of rather large cross-section (35 cm x 50 cm) was used to determine the number of primary electrons that are needed for the calculation of $R$ to have a given level of statistical uncertainty (2%). In these simulations, the distance off the central beam axis within which the energy was scored, $r$, and the step in beam incidence angle, $\Delta\vartheta$, were varied as follows: $r = 5$ mm or 2 cm and $\Delta\vartheta = 5°$ or $10°$. It was found that reducing the angle step had no effect in the calculation. Moreover, the results of the simulation were similar for the two values of $r$. The conclusion of these test simulations was that, for $r = 2$ cm and $\Delta\vartheta = 10°$, 10 million primary electrons should be simulated at all angles of incidence except at zero angle, where four times this statistics was required, if the above mentioned statistical accuracy of $R$ is aimed at.

Simulations of the rotational depth dose and $R_{MC}$ distributions were then performed for smaller phantom dimensions, namely an ellipsoid of cross section 20 cm x 40 cm and one cylinder of 30 cm diameter. It was found that both distributions depend on the phantom dimensions and that the factor $R_{MC}$ has an almost linear dependence on depth. In all cases, the rotational depth dose seemed to have overestimated values at the phantom surface.

The possibility that the high surface dose is due to the production cuts was investigated by defining a region of lower production cuts about the volume where the energy scoring was done. The production threshold for secondary electrons was reduced in this volume from 100 keV to 10 keV, while the 100 keV threshold was kept in the remaining volume of the phantom. This seemed to remove almost completely the dose excess at the surface, which also appeared to be due to contributions from high angles of beam incidence. The 10 keV calculation seemed also to agree better with the VMC++ distribution at SSD = 100 cm. The low-threshold calculation was then used to calculate the absorbed dose delivered at the prescription depth in one rotation.

A previous UMAS study [8] was performed for the degraded beam of a Varian Clinac 2100C, where the value of $R$ at the surface of a cylindrical phantom was measured with ionisation chambers, diodes and TLDs. The measured values were between 0.65 and 0.97. The low-production threshold calculation for the same geometry (cylindrical phantom) in this study gave a surface value of 0.69 for $R_{MC}$, i.e. a value in the same interval as the previous measurements despite the difference in energy spectrum.

Requiring an upper limit for the allowed step length is an option that was not used in the present simulations. Moreover, the energy scoring grid was not built in the geometry of the simulated phantom, so that the tracking was allowed to proceed without being aware of the dimensions of this grid. These two options may be the reason for the cut dependence of the simulation results observed in this study. It would be of interest to determine whether a restriction in the step length would remove this dependence so that more accurate calculations could be done without using low production thresholds.

## 3.12  Conclusion

This theoretical study has shown that it is possible to use Geant4 to model the relation between the stationary and rotational depth dose distribution so as to improve the accuracy of the absorbed dose delivered during treatment by determining the number of rotations needed for a specific surface dose.

# APPENDIX: APPLICATION DIAGRAMS

The following classes were defined in the present application:
- DetectorConstruction (volume and material definitions)
- PrimaryGeneratorAction (primary electron generation)
- SteppingAction (step information handling/energy scoring)

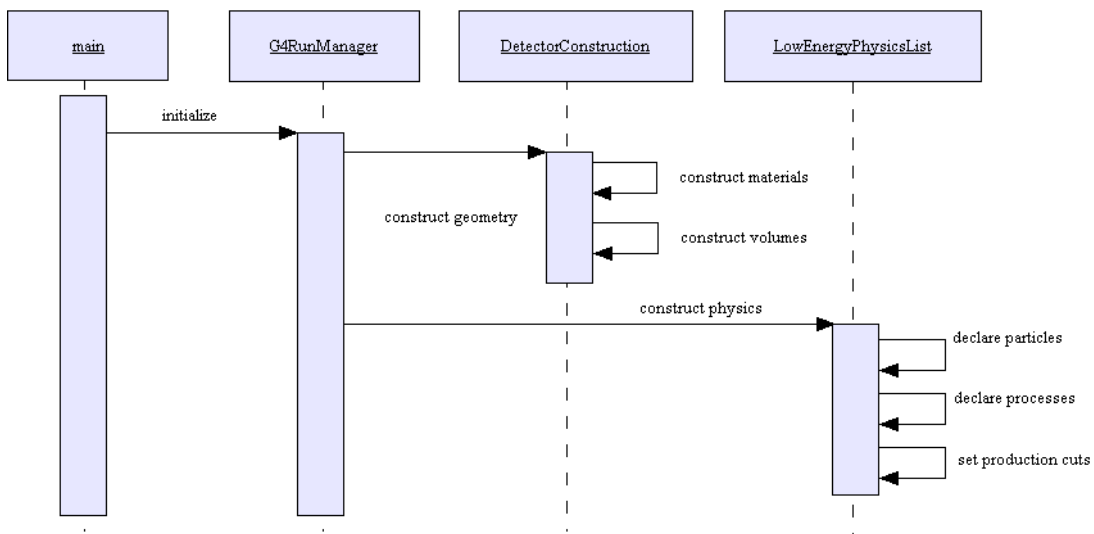The structure of the program is illustrated in the diagrams below.
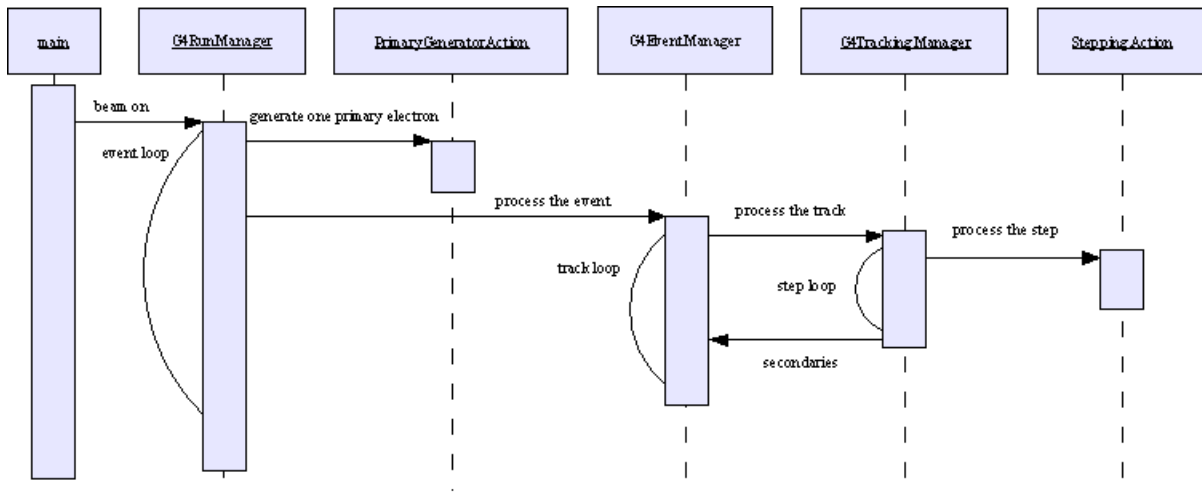


**Figure A.1.** Initialization of the run.



**Figure A.2.** How the run proceeds. The energy depositions are saved in histograms in the SteppingAction class.

# ACKNOWLEDGEMENTS

# REFERENCES

[1] A. Ravi et al., *Total skin electron beam therapy in the management of cutaneous malignancies*, Clinics in Dermatology, 2001;19:354-356.

[2] F. M. Khan, *The physics of radiation therapy*, Lippincott Williams & Wilkins, 2003.

[3] C. Freeman et al., *Clinical experience with a single field rotational total skin electron irradiation technique for cutaneous T-cell lymphoma*, Radiotherapy and Oncology, 24 (1992) 155-162.

[4] E. Podgorsak et al., *Physical aspects of a rotational total skin electron irradiation*, Med. Phys. 10 (2), Mar/Apr 1983.

[5] K. Müller-Sievers et al., *Dosimetry of rotational partial-skin electron irradiation*, Radiotherapy and Oncology 58 (2001) 187-192.

[6] P. Kumar et al., *Rotational total skin electron beam therapy, Strahlentherapie und Onkologie,* 164 (1988) 73-78.

[7] P. Kumar et al., *Dosimetry of rotational versus multifield total-skin electron-beam therapy (TSEBT) techniques*, Radiation Medicine, Vol. 5, No 2, pp. 51-54, 1987.

[8] L. Wittgren and M. Lööf, *Inmätning av helkroppselektroner på Clinac 2100C med high dose rate elektroner och roterande plattform*, RADFYS 94:06, Radiofysikavdelning, UMAS.

[9] S. Agostinelli et al., *Geant4 - a simulation toolkit*, Nuclear Instruments and Methods in Physics Research Section A: Accelerators, Spectrometers, Detectors and Associated Equipment, Volume 506, Issue 3, 1 July 2003, pp. 250-303.

[10] L. Beaulieu et al., *Overview of Geant4 applications in medical physics*, Proceedings of IEEE-NSS, Portland, 2003.

[11] E. Traneus, private communication.

[12] Geant4 physics reference manual,
http://geant4.web.cern.ch/geant4/G4UsersDocuments/UsersGuides/
PhysicsReferenceManual/html/PhysicsReferenceManual.html.

[13] S. Chauvie et al., *Geant4 electromagnetic physics*, INFN/AE-00/07.

[14] S. Chauvie et al., *Geant4 low energy electromagnetic physics*, Proceedings of CHEP2001, Beijing, 2001.

[15] K. Amako et al., *Validation of Geant4 electromagnetic physics versus protocol data*, Proceedings of IEEE-NSS, Rome, 2004.

[16] G. Cirrone et al., *Precision validation of Geant4 electromagnetic physics*, Proceedings of IEEE-NSS, Portland, 2003.

[17] H. W. Lewis, *Multiple scattering in an infinite medium*, Phys. Rev. 78 (1950) 526.

[18] Evaluated Photon Data Library (EPDL),
http://www.llnl.gov/cullen1/photon.htm.

[19] Evaluated Electron Data Library (EEDL),
http://www.llnl.gov/cullen1/electron.htm.

[20] Evaluated Atomic Data Library (EADL),
http://www.llnl.gov/cullen1/atomic.htm.

[21] J. Apostolakis et al., *Geant4 low energy electromagnetic models for electrons and photons,* CERN-OPEN-99-034 and INFN/AE-99/18, 1999.

[22] Y. S. Tsai, *Pair production and bremsstrahlung of charged leptons*, Rev. Mod. Phys. 46 (1974) 815.

**[23]** IAEA (2004), *Absorbed dose determination in external beam radiotherapy: an international code of practice for dosimetry based on Standards of Absorbed Dose to Water*, Technical Report Series No. 398.

**[24]** AAPM (1990), American Association of Physicists in Medicine, *Clinical electron-beam dosimetry*, Report of AAPM Radiation Therapy Committee Task Group No 25 (American Institute of Physics, New York).

**[25]** ICRU (1984), *Stopping Powers for Electrons and Positrons*, Report No. 37, Bethesda, MD: International Commission on Radiation Units and Measurements.

**[26]** I. Kawrakow, *VMC++, Electron and Photon Monte Carlo Calculations Optimized for Radiation Treatment Planning*, Advanced Monte Carlo for Radiation Physics, Particle Transport Simulation and Applications: Proceedings of the Monte Carlo 2000 Conference, Lisbon, 23-26 October, 2000. Springer, Berlin, 2001, eds. A. Kling, F. Barao, M. Nakagawa, L. Travora and P. Vaz.

**[27]** S. Almehed, private communication.